




Dislocation-mediated and twinning-induced plasticity of CoCrFeMnNi in varying tribological loading scenarios

Antje Dollmann^{1,2}, Alexander Kauffmann¹, Martin Heilmaier¹, Aditya Srinivasan Tirunilai¹, Lakshmi Sravani Mantha^{3,4}, Christian Kübel^{3,4,5}, Stefan J. Eder^{6,7}, Johannes Schneider^{1,2}, and Christian Greiner^{1,2,*} 

¹Institute for Applied Materials (IAM), Karlsruhe Institute of Technology (KIT), Kaiserstraße 12, 76131 Karlsruhe, Germany

²MicroTribology Center (μ TC), Straße am Forum 5, 76131 Karlsruhe, Germany

³Institute of Nanotechnology (INT), KIT, 76344 Eggenstein-Leopoldshafen, Germany

⁴KIT-TUD-Joint Research Laboratory Nanomaterials, Technical University Darmstadt (TUD), 64287 Darmstadt, Germany

⁵Karlsruhe Nano Micro Facility (KNMF), KIT, 76344 Eggenstein-Leopoldshafen, Germany

⁶AC2T Research GmbH, Viktor-Kaplan-Straße 2/C, 2700 Wiener Neustadt, Austria

⁷Institute of Engineering Design and Product Development, TU Wien, Lehárgasse 6, Objekt 7, 1060 Vienna, Austria

Received: 16 December 2021

Accepted: 25 June 2022

© The Author(s) 2022

ABSTRACT

Coarse-grained, metallic materials undergo microstructure refinement during tribological loading. This in turn results in changing tribological properties, so the microstructural evolution is a parameter which should not be underestimated while designing tribological systems. Single-trace experiments were conducted to understand the initiation of deformation mechanisms acting in various tribological systems. The main scope of this work was to investigate the influence of normal and friction forces as well as crystal orientations on the dominating deformation mechanism in a face-centred cubic concentrated solid solution. While varying the normal force is easily realised, varying friction forces were achieved by using several counter body materials paired against CoCrFeMnNi. The subsurface deformation layer was either mediated through dislocation slip or twinning, depending on the grain orientation and on the tribological system. A layer dominated by dislocation-based deformation is characterised by lattice rotation, the formation of a dislocation trace line or subgrain formation. Such behaviour is observed for tribological systems with a low friction coefficient. For systems dominated by deformation twinning, three types of twin appearance were observed: small twins interacting with the surface, large twins and grains with two active twin systems. Two different twinning mechanisms are discussed as responsible for these characteristics.

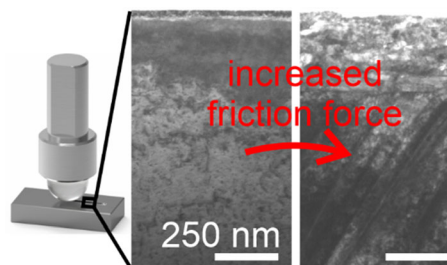
Handling Editor: Avinash Dongare.

Address correspondence to E-mail: greiner@kit.edu

<https://doi.org/10.1007/s10853-022-07661-3>

Published online: 14 September 2022

GRAPHICAL ABSTRACT



Introduction

Previous research has shown that for metals in a tribological contact, a feedback loop exists between the friction coefficient, the stress state and the microstructure [1]. During a tribological experiment, the friction and the normal force determine the stress state that leads to a microstructural evolution in the subsurface area [2, 3]. In turn, the resulting deformation layer leads to a change in the friction coefficient. So far, various microstructural characteristics have been observed in coarse grained, face-centred cubic (fcc) metallic materials under tribological load, such as a dislocation trace line [4, 5], subgrain formation [2, 6], deformation twinning [7, 8], band-like patterns [9–11] and nanocrystalline grains [7, 12].

In essence, a tribological system features two forces controlling the microstructural evolution: first, the normal force, which can be easily adjusted and second, the friction force, which is a function of the tribological system itself. Further parameters determining the deformation layer are cycle number [4, 13, 14], sliding velocity [15, 16], temperature [16] and ambient environment [17].

The quinary single phase high-entropy alloy (HEA) CoCrFeMnNi [18], exhibiting a medium stacking fault energy, was chosen as the material of interest because it covers dislocation-mediated microstructures at low strains and twin-induced plasticity at higher strains, although this knowledge stems from uniaxial load experiments [19, 20]. To the authors' best knowledge, only three other research groups have investigated the tribological properties of single phase CoCrFeMnNi so far. Ayyagari et al. analysed

the wear behaviour in dry and marine environments [21]. Joseph et al. [22] investigated the friction and wear behaviour at temperatures ranging from room temperature up to 900 °C. Jones et al. examined the interplay between grain refinement and the friction and wear behaviour after several thousand sliding cycles [12]. The two normal loads they applied resulted in different grain sizes in the subsurface area [12]. In our earlier work, we analysed the microstructural evolution with increasing cycle number with a focus on the onset of microstructural changes at high friction coefficients [7]. In contrast, the influence of the friction and normal force is investigated after a single-trace experiment in this manuscript. Besides that, the pronounced adhesive tendency of CoCrFeMnNi enables us to cover friction coefficients between 0.1 and 1 by using different counter body materials and environments. Furthermore, the influence of an increased normal load is investigated.

The polycrystallinity of CoCrFeMnNi makes it necessary to take the crystal orientation into account. It is known from uniaxial tests that the initial grain orientation is decisive for the occurrence of deformation twinning [23, 24]. In contrast to high SFE materials [25–27], there is only little data available on medium SFE materials [7, 13, 28]. For example, nanoscratch tests in austenitic steel have demonstrated the influence of the initial crystal direction parallel to the normal direction on the formation of slip traces next to the wear track, pile-up and the wear track depth [28]. Hence, with the study of polycrystalline CoCrFeMnNi, it is a further goal of this manuscript to draw conclusions about the

relation between the active deformation mechanism and the crystal orientation under tribological load.

Materials and methods

CoCrFeMnNi was manufactured via arc-melting, homogenised, cold-rolled and heat treated as described elsewhere [7]. An average grain size of about 40 μm (excluding recrystallisation twins) was measured by the linear intercept method. The chemical composition was determined via inductively coupled plasma optical emission spectrometry (ICP-OES) to 15.2 at.% Co, 21.7 at.% Cr, 21.2 at.% Fe, 21.2 at.% Mn and 20.1 at.% Ni (accuracy of 0.1 at.%). To ensure a defect-free surface, the samples were ground up to a grit of P4000, polished with diamond suspensions of 3 μm and 1 μm (Cloeren Technology GmbH, Wegberg, Germany) for at least eight minutes each, and finally electropolished with an electrolyte composed of perchloric acid and methanol in a ratio of 1:9. Images of the defect-free surface are given in Ref. [7]. A surface roughness of $S_a = (80 \pm 10)$ nm was achieved with the described procedure. The measurements were carried out interferometrically with a PLu neox instrument (Sensofar, Barcelona, Spain).

The tribological experiments were conducted with a custom-built tribometer encapsulated in a climate-controlled chamber. The load application was done with dead weights to limit out effects of the samples skewness and kurtosis. Counter body spheres with a diameter of 10 mm made of sapphire (Saphirwerk, Switzerland), SiC (hightech ceram, Dr. Steinmann + Partner GmbH, Germany) and Si_3N_4 (Saint-Gobain Ceramic Materials GmbH, Germany) were used. The surface roughnesses S_a are (14 ± 2) nm for sapphire, (20 ± 4) nm for Si_3N_4 and (60 ± 12) nm for SiC, interferometrically measured.

All experiments were conducted in a single-trace fashion. This means that the CoCrFeMnNi sample and counter sphere were brought into contact and loaded, the stage, on which the CoCrFeMnNi sample was mounted, moved for 12 mm. Afterwards the counter sphere was lifted up. Wear tracks with counter spheres out of Si_3N_4 , SiC and sapphire were produced with a normal load of 2 N in air with $(50 \pm 3)\%$ relative humidity (RH). For a further variety in friction coefficient, the experiments with a SiC and sapphire sphere were conducted in N_2 atmosphere. The influence of normal force was tested

by loading a SiC sphere with a normal load of 5 N in air with $(50 \pm 3)\%$ RH. All experiments were performed at room temperature and a sliding velocity of 0.5 mm/s.

The wear volume was measured interferometrically at the positions 0 mm, 3 mm, 6 mm, 9 mm and 12 mm. These volumes were averaged and divided by the image width resulting in the wear volume per μm . The wear tracks were further analysed and using a dual beam focused ion beam (FIB), scanning electron microscope (Helios NanoLabTM DualBeamTM 650, ThermoFisher, Hillsboro, USA). TEM foils were cut parallel to the sliding direction in the middle of the wear track in a process with negligible ion beam damage [29]. Images were taken in STEM mode in the SEM. Additional analyses were conducted using on-axis transmission Kikuchi diffraction (TKD). The scans were performed with an acceleration voltage of 30 kV, a current of 0.8 nA and a step size of 5 nm. The patterns were recorded by an e-flash^{HD} detector with the OptimusTM TKD head and analysed using Esprit 2.1 (all by Bruker, Billerica, USA). These data were further analysed with the Matlab toolbox MTEX [30].

High-resolution transmission electron microscopy (HRTEM) images were obtained using an (image) aberration-corrected Titan 80–300 (ThermoFisher Scientific, Hillsboro, USA) operated at 300 kV and equipped with a Ultrascan 1000 CCD camera (Gatan, Pleasanton, USA). These images are average background subtraction filtered (ABSF) in DigitalMicrograph® [31].

Results

The various tribological systems investigated here were selected to result in varying friction coefficients (μ). The friction coefficients as a function of sliding distance for the single trace experiments are given in Fig. 1 for all six systems. A colour was assigned to each tribological system. The system SiC/2N/air is colour-coded in green, SiC/2N/ N_2 in blue, sapphire/2N/ N_2 in purple, sapphire/2N/air reported in [7] in orange, Si_3N_4 /2N/air in black and SiC/5N/air in red.

SiC spheres paired with CoCrFeMnNi result in the lowest observed friction coefficients, independent of atmosphere or applied normal load, and maintained an almost constant friction coefficient with sliding distance. The change from air with 50% RH to dry N_2

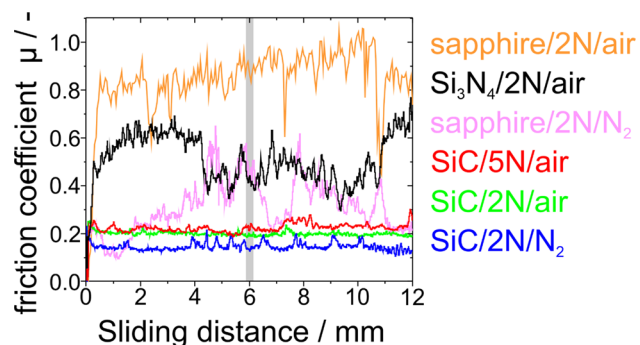


Figure 1 Friction coefficients as a function of the sliding distance. The position at a sliding distance of 6 mm is marked, as this is the TEM foil lift-out position. The data for sapphire/2N/air (orange) is taken from [7].

causes a small decrease in the friction coefficient at a normal load of 2 N. The increase in normal load from 2 to 5 N in air with 50% RH results in a similar friction coefficient. The tribological systems sapphire/2N/N₂ and Si₃N₄/2N/air exhibit a varying friction coefficient with increasing sliding distance. Interestingly, both tribological systems have the same friction coefficient at a sliding distance of 6 mm, which is the STEM foil lift-out position. The highest friction coefficient was measured for the system sapphire/2N/air [7].

SE images of the wear tracks and the contact area on the spheres are given in Fig. 2. The dots next to the wear track are oxides resulting from the manufacturing routine. The position of these oxides can be also seen within the wear tracks with SiC sphere as counter body and a normal load of 2 N (Fig. 2a + b). With a SiC sphere as counter body and 5 N, these locations cannot be seen as the wear track is too deep. None of the SiC spheres independent of normal load or atmosphere shows transferred material of CoCrFeMnNi. Whereas clear patches of transferred material can be seen on the sphere out of Si₃N₄ and sapphire (Fig. 2 c2, d2 and e2). Additionally, flakes can be observed within the wear tracks (Fig. 2 c1, d1 and e1). The wear volumes are $(13.1 \pm 5.6) \mu\text{m}^3/\mu\text{m}$ for Si₃N₄/2N/air, $(8.7 \pm 5.1) \mu\text{m}^3/\mu\text{m}$ for sapphire/2N/N₂, $(42.8 \pm 14.3) \mu\text{m}^3/\mu\text{m}$ for sapphire/2N/air and $(8.7 \pm 1.3) \mu\text{m}^3/\mu\text{m}$ for SiC/5N/air. The wear volumes of SiC/2N/air and SiC/2N/N₂ could not be measured, as the wear tracks could not be clearly differentiated from the surface roughness.

In Fig. 3, the cross-sectional STEM images of each tribologically loaded CoCrFeMnNi system are given.

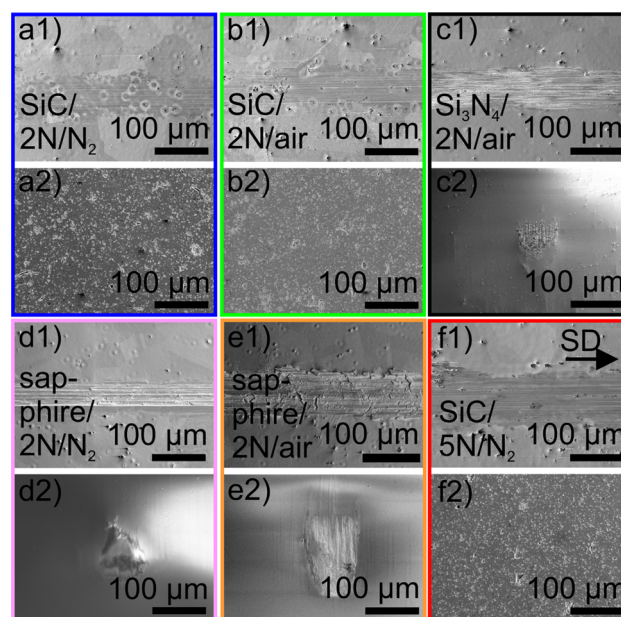


Figure 2 Images of the wear tracks and counter bodies after single trace experiments with a velocity of 0.5 mm/s on CoCrFeMnNi. All images with a 1 in the label show the wear tracks, and with a 2 the contact area of the counter body. The sliding direction is from left to right in the wear tracks. The following systems are shown: a SiC/2N/N₂, b SiC/2N/air, c Si₃N₄/2N/air, d sapphire/2N/N₂, e sapphire/2N/air [7] and f SiC/5N/N₂.

No image of the microstructure after the sapphire/2N/air experiment is given as the resulting microstructure is analysed in detail in [7]. The color-coding from Figs. 1 and 2 is also used in Fig. 3. As for some systems two grains are analysed different shades of the same colour were used. This colour-coding for the considered tribological systems and grains is used throughout the entire manuscript. The friction coefficient, determining the microstructures observed using (S)TEM is as mentioned before after a sliding distance of 6 mm.

Images of the subsurface deformation layer in two grains of the experiment with SiC/2N/air are presented in Fig. 3a + b to investigate the initial grain orientation. The microstructure in Fig. 3a is characterised by a bright horizontal line at a depth of $(26 \pm 5) \text{ nm}$. In contrast, nearly vertical line-type features occur down to a depth of $(163 \pm 49) \text{ nm}$ in Fig. 3b. The bands are slightly tilted in sliding direction (SD). The subsurface deformation layer for the experiment with SiC/2N/N₂ is given in Fig. 3c. The STEM foil includes two grains, and the initial grain boundary is marked in the image. The microstructure is dominated by a line starting at the

surface in the left grain, crossing the initial grain boundary and proceeding into the right grain down to a depth of 290 nm. A horizontal line is observed closer to the surface marked by a black arrow. The microstructure after the experiment with sapphire/2N/N₂ in Fig. 3d consists of a nanocrystalline layer directly in the sub-surface area and line-type characteristics tilted in SD.

In the tribological system Si₃N₄/2N/air, two sets of line-type characteristics are observed in one grain, as seen in Fig. 3e. Here, one line is again tilted in SD and the other opposite to SD, both marked in white colour. In the other grain in Fig. 3f, no clear characteristics can be seen. Two grains of the experiment SiC/5N/air show a horizontal line. In the grain in Fig. 3g, the line is at a depth of (244 ± 15) nm and in the grain in Fig. 3h at (98 ± 5) nm.

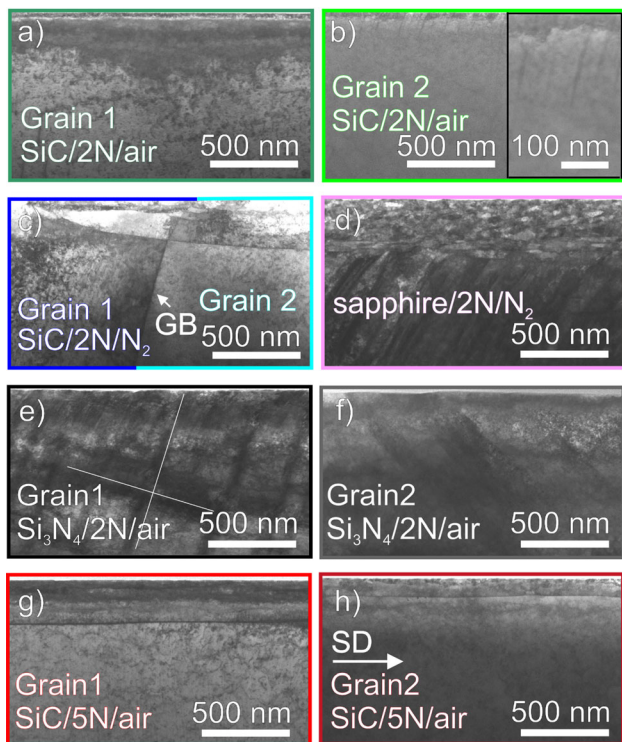


Figure 3 STEM images of the various tribological systems. **a** and **b** STEM images of the microstructures from the SiC/2N/air (green) experiment for two different grains. In **b** a zoom-in of the near-surface area is marked by a black rectangle. **c** STEM image of the microstructure from the SiC/2N/N₂ (blue) experiment, **d** sapphire/2N/N₂ (purple), **e** and **f** Si₃N₄/2N/air (black/grey) in two different grains and **g** and **h** SiC/5N/air (red) in two different grains. All STEM images were cut in the middle of the wear track parallel to the sliding direction (SD). The SD is from left to right.

The described deformation layers are further analysed by transmission Kikuchi diffraction (TKD) and HRTEM. In Fig. 4a–f, TKD measurements of the STEM images in Fig. 3a + b of the experiment SiC/2N/air are presented.

Both measurements are colour-coded in sliding (SD), normal (ND) and transverse direction (TD). Furthermore, MTEX was employed to detect the different types of grain boundaries. Grain boundaries with a small-angle boundary character (SAGB) (3° to

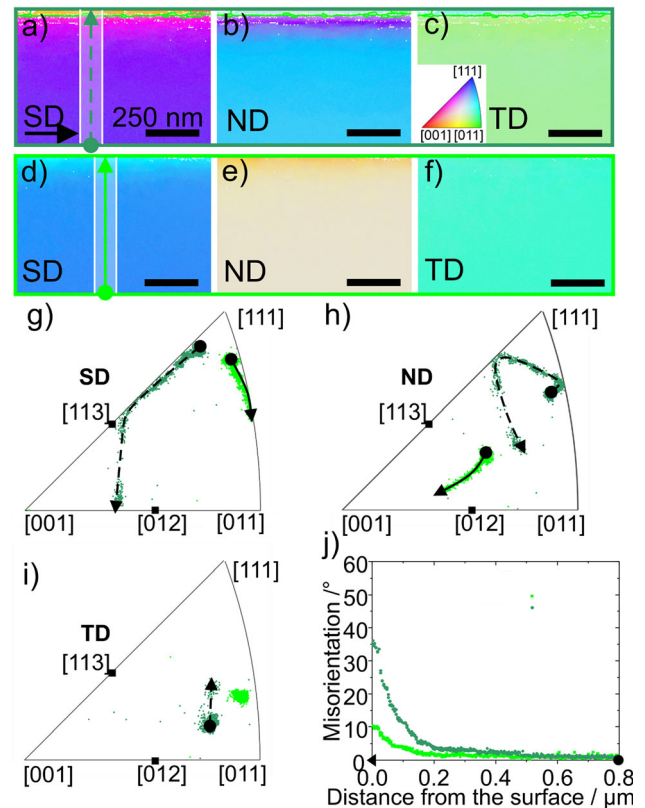


Figure 4 Crystal orientation influence for the same applied stress state (SiC/2N/air). **a** to **c** TKD measurement of the grain shown in Fig. 3a, colour-coded in sliding (SD), normal (ND) and transverse direction (TD), respectively. **d** to **f** TKD measurement of the grain in Fig. 3b, colour-coded in SD, ND and TD. The colour-coding is given in the inset in (c). Small-angle grain boundaries (3–15°) are highlighted in green, high-angle grain boundaries (> 15°) in red and twins (Σ 3) in blue. The SD is from left to right. The orientation data between the white lines in (a) and (d) were plotted in **g** to **i** in inverse pole figures (IPFs) in SD, ND and TD, respectively. Dark green data points belong to the grain presented in (a) to (c) and in light green to (d) to (f). The dot marks the orientation in the bulk, and the arrowhead marks the orientation at the surface. The arrows within the IPFs point towards the surface. **j** Misorientation profile along the arrows in (a) and (d). The distance 0 μ m marks the surface.

15°) are coloured in green, with a high-angle character (HAGB) ($> 15^\circ$) in red and twins ($\Sigma 3$) in blue. The horizontal line in Fig. 3a was identified as a SAGB in Fig. 4a–c. A colour-gradient is seen beneath the SAGB with increasing distance from the surface. The line-type characteristics in Fig. 3b could not be resolved in Fig. 4d–f, instead a colour-gradient is observed.

The crystal orientations between the white lines in Fig. 4a + d are plotted in inverse pole figures (IPFs) in Fig. 4g–i in SD, ND and TD, respectively. The grain orientations farthest away from the surface are marked by a circle and are interpreted as the initial grain orientations. The orientations at the surface are marked by arrow heads. The dashed line represents the data points of the grain in Fig. 4a, and the solid line the data points of the grain in Fig. 4d. The initial crystal directions parallel to SD are both close to the [111] pole in Fig. 4g. Both crystal directions move along a bisector with decreasing distance to the surface. The crystal direction parallel to SD of the grain in Fig. 4a moves along the [001]–[111] bisector, leaving the bisector close to a [113] direction, rotating towards the [001]–[011] bisector. The crystal direction of the grain in Fig. 4d moves along the [011]–[111] bisector in Fig. 4g. The crystal direction parallel to ND in Fig. 4h of the grain in Fig. 4b is reflected twice at two different bisectors, whereby the crystal direction parallel to ND of the grain in Fig. 4e rotates from the centre of the IPF into the direction of the [001] pole. The crystal direction parallel to TD in Fig. 4i changes only a little for both grains. The misorientation was calculated in reference to the initial grain orientation. Misorientation profiles were extracted along the arrows in Fig. 4a + d and plotted in Fig. 4j. The one of the grain in Fig. 4a exhibits a discontinuity smaller than 10° and has a maximum misorientation at the surface of 35° . In contrast, the profile of the grain in Fig. 4d is continuous and exhibits a maximum misorientation of 10° . Both grains have in common that the increase in misorientation starts at a depth of around $0.5 \mu\text{m}$.

The line-type features in Fig. 3b were further investigated using HRTEM. The result of this analysis is given in Fig. 5. In three different regions with increasing distance to the surface, fast Fourier transformation (FFT) analyses were performed in order to investigate the possible occurrence of twinning. The blue dashed line in the FFT images connects the diffraction spots for the matrix, while the red dashed

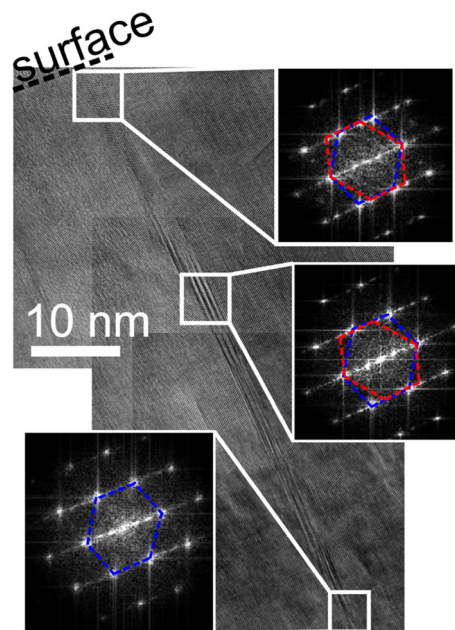


Figure 5 HRTEM image of the line-like characteristics presented in Fig. 3b. The samples surface is marked by a dashed black line. In the areas marked by white squares, FFT analyses were carried out. In the FFT, the twins are indicated by dashed red lines and the matrix by dashed blue lines. The sliding direction was from left to right.

line connects the diffraction spots of the twins. In the regions closer to the surface, the twin is unambiguously detected, which is not the case for the area farthest from the surface. The twinned area is thicker close to the surface than in the bulk also seen by surface steps in the twin boundary. Furthermore, the twin itself has not a perfect crystal structure.

The TKD measurements of the microstructures showing a horizontal line (Fig. 3c, g + h) are presented in Fig. 6. All the horizontal lines were detected as SAGB except the one in Fig. 6g–i. Above the horizontal lines colour-gradients and (sub-)grains are observed. The misorientation profile in Fig. 6j were extracted along the arrows in Fig. 6a, d, g. In all profiles, discontinuities are present.

The depth of the discontinuity in the right grain of the SiC/2N/N₂ experiment (bright blue) and in grain in the SiC/5N/air experiment in Fig. 6d (bright red) is nearly the same. The discontinuity in the left grain for the SiC/2N/N₂ experiment (dark blue) is closer to the surface and the discontinuity for the grain in the SiC/5N/air experiment in Fig. 6g (dark red) is the closest to the surface. The magnitudes of these

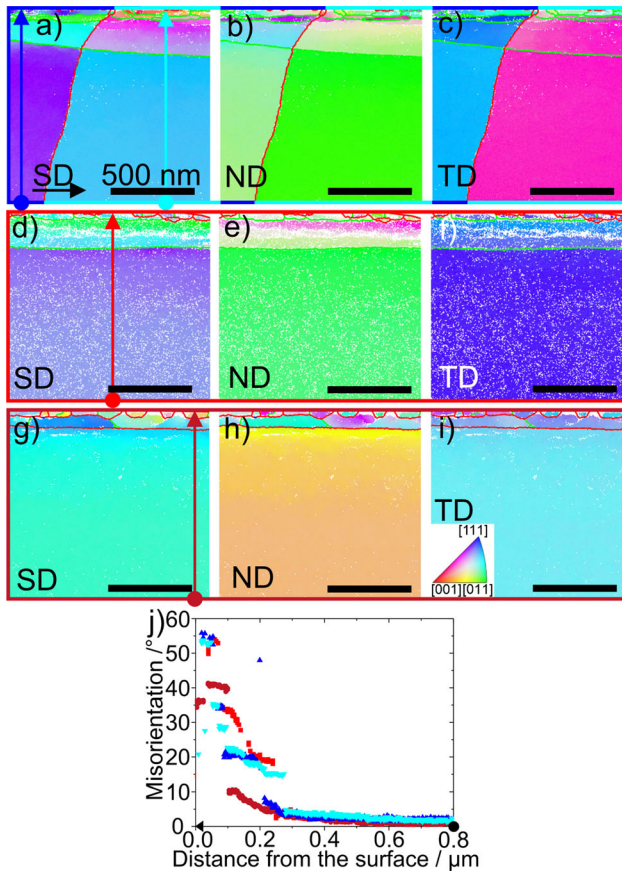


Figure 6 Deformation layers with dislocation trace line. **a** to **c** TKD measurement of the grain shown in Fig. 3c after the SiC/2N/N₂ experiment, **d** to **f** TKD measurement of the grain shown in Fig. 3g after the SiC/5N/air experiment, **g** to **i** TKD measurement of the grain in Fig. 3h after the SiC/5N/air experiment. All measurements are colour-coded in SD, ND and TD. The colour-coding is given in the inset in (i). Small-angle grain boundaries (3–15°) are highlighted in green, high-angle grain boundaries (> 15°) in red and twins (Σ 3) in blue. The SD is from left to right. **j** gives the misorientation profiles along the arrows in (a, d, g).

discontinuities are the largest for the SiC/5N/air experiment.

The TKD measurements with superimposed grain boundary analyses of the experiments with sapphire/2N/N₂ (Fig. 3d) and Si₃N₄/2N/air (Fig. 3e) are given in Fig. 7. The microstructure of the sapphire/2N/N₂ experiment (Fig. 6a–c) is characterised by nanocrystalline grains in the subsurface area as well as by twins. The two regions are separated from each other by a SAGB. The nanocrystalline grains become coarser with increasing distance to the surface. The twins exhibit lenticular shape, hence, being thinner at their ends than in the centre. The subsurface region of the experiment Si₃N₄/2N/air (Fig. 7d–

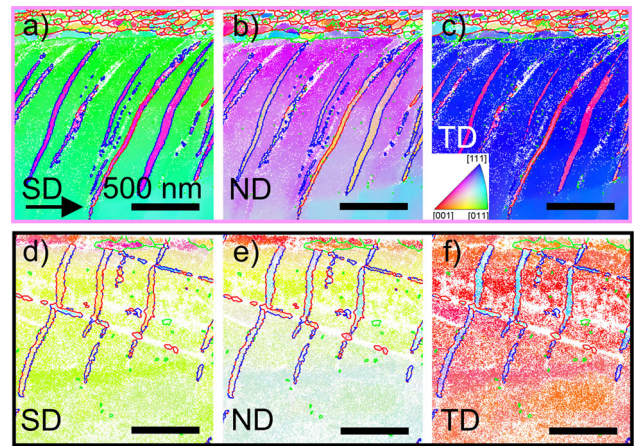


Figure 7 Types of twin appearances. **a** to **c** TKD measurement of the experiment for sapphire/2N/N₂ (STEM in Fig. 3d) and **d** to **f** Si₃N₄/2N/air (STEM in Fig. 3e). The measurements are colour-coded in SD, ND and TD. The colour-coding is given in the inset in (c). Small-angle grain boundaries (3–15°) are highlighted in green, high-angle grain boundaries (> 15°) in red and twins (Σ 3) in blue. The sliding direction is from left to right.

e) exhibits a layer with grains separated by SAGBs beneath the surface, and with increasing distance to the surface two twin systems are detected. The line-type characteristics (see Fig. 3d) exhibits twin and high-angle grain boundaries.

The TKD measurement of the second grain from the experiment Si₃N₄/2N/air (Fig. 3f) is given in Fig. 8. In contrast to all the other observed grains, only a colour gradient and not a horizontal line nor twins can be observed.

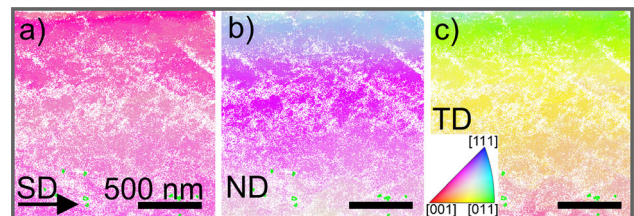


Figure 8 TKD measurement of the second grain of Si₃N₄/2N/air (STEM in Fig. 3f). **a** to **c** colour-coded in SD, ND and TD, respectively. The colour-coding is given in the inset in (c). Small-angle grain boundaries (3–15°) are highlighted in green, high-angle grain boundaries (> 15°) in red and twins (Σ 3) in blue. The sliding direction is from left to right.

Discussion

This manuscript investigates the influence of a range of tribological systems on the frictional properties and especially on the subsurface microstructure in order to answer the following questions: How do friction and normal load change the tribology-induced microstructural evolution? Which are the characteristics and formation mechanisms of the observed microstructures developing under varying tribological loads? Which role does the initial grain orientation play?

Variation of friction forces

The tribologically imposed stress states of the materials constituting the contact is a function of the friction coefficient [1, 32]. To investigate the effect of the stress state on the microstructural evolution, the tribological systems were varied to achieve varying friction coefficients, see Fig. 1. Steady-state friction coefficients are already published in literature for several tribological systems containing CoCrFeMnNi [12, 21, 22], which are similar to the friction coefficients in the present study. The obtained variation of the friction coefficients stems from various contributions as briefly discussed below.

The work of adhesion is considered in the first place, which comprises the surface free energies of the two materials and their interface [33]. Neither the surface free energy of CoCrFeMnNi nor the ones of the interfaces are published in literature to the best of the authors' knowledge. The values of the surface free energy of the counter body materials [34] do not directly correlate with the measured friction coefficients. No final conclusion can therefore be drawn on the influence of the work of adhesion on the friction coefficient in the chosen tribological systems. However, wear tracks with a low friction coefficient have a scratched appearance, and flake formation was observed in wear tracks with a high friction coefficient (Fig. 2). Furthermore, the contact areas of the counter bodies with a high friction coefficient exhibit material transfer. Flake formation and material transfer are clear indicators of adhesive wear [33]. These factors therefore provide a qualitative indication of different adhesive forces within the chosen tribological systems, but the adhesive forces will not be further analysed in the current manuscript.

The second parameter is the surface roughness of the different counter body materials. It was proposed in literature [35–37] that with an increasing surface roughness the contact area decreases, which can result in a lower friction coefficient. This tendency was confirmed in our experiments.

The environmental changes from air with 50%RH to dry N₂ resulted in a lower friction coefficient. Surface softening was reported for sapphire with increasing humidity [38][38] which can facilitate shearing of the surface and lead to an increased contact area [40]. These two effects might therefore cancel each other out [40].

Three aspects, namely adhesive force, surface roughness and surface softening, were considered to explain the varying friction coefficients. So far, it is unclear to which extent they contribute to the friction forces.

Influence of initial grain orientation

The initial grain orientation can strongly influence the deformation mechanism, especially in the case of deformation twinning under uniaxial load [23, 24]. The influence of the initial grain orientation under tribological load was investigated by comparing two subsurface deformation layers for the same tribological system and, therefore, also the same applied surface stress state.

The tribological system in focus was chosen to be SiC/2N/air, as it does not exhibit material transfer and the friction coefficient is nearly constant over the entire sliding distance (see Fig. 1). The two grains in question were presented in Fig. 3a + b and Fig. 4, demonstrating their different microstructural evolution. The thickness of the tribologically induced subsurface layer is small for both grains, so the orientation underneath this deformed layer was interpreted as the initial grain orientation (see TKD results in Fig. 4).

The SAGB identified in Fig. 4a has been described as a dislocation trace line (DTL) in earlier publications [4, 5, 13]. The DTL in CoCrFeMnNi will be further discussed in the subsection 'Dislocation trace line and crystal rotation'. The line-type features in Fig. 3b were clearly identified as twins using FFT in Fig. 5. Therefore, there is a need for understanding why plastic deformation is mediated by dislocation slip in one grain and twinning-induced plasticity in the other; under otherwise identical tribological

conditions. The initial grain orientation as well as the type of applied load is decisive for deformation twinning [24]. The loading was the same for both grains. The initial crystal directions of the two grains are quite close to each other parallel to SD and TD (Fig. 4g + i). Thus, it is evident that the initial crystal direction parallel to ND under the given loading parameters is decisive for the dominating deformation mechanism. This is unexpected, as it was demonstrated in a previous study that the initial grain direction parallel to SD is decisive for the occurrence of deformation twinning [7]. The differences between the published results in [7] and the results in Fig. 4 are the selected counter body materials, resulting in a significantly reduced friction coefficient and no material transfer here and in a higher friction coefficient and material transfer in [7]. The lack of material transfer results in lower adhesive forces, which in turn decrease the tensile stresses parallel to SD at the trailing edge of the counter body. Further details about the twinning mechanism under tribological load are discussed in the section ‘Twinning’.

The increase in misorientation in Fig. 4j is caused by dislocation motion. In both grains this increase starts at $0.5\ \mu\text{m}$, which shows that the critical resolved shear stress (CRSS) for dislocation glide is reached at a similar depth. A difference between the two grain orientations can be observed in the maximum misorientation from the bulk to the surface which, is approximately 25° higher in the grain with the DTL than in the grain with twins. The misorientation profiles (Fig. 4j), however, only include the misorientation changes caused by dislocation motion. This indicates a difference in the dislocation activity. The discontinuity in misorientation corresponds to the SAGB in the grain shown in Fig. 4a–c. The higher the misorientation, the more dislocations are stored in the lattice. The formation of a SAGB leads to a reduction in the stored lattice energy, therefore the discontinuity could be favoured [41].

The two investigated grains under the same tribological loading reveal that not only the stress state, but also the initial grain orientation can be decisive for the dominating deformation mechanism under tribological load.

Influence of a higher normal load

For medium stacking fault energy materials like CoCrFeMnNi, increasing the stress under uniaxial loading increases the probability for the material to twin. We therefore expected to observe more and larger twins at a normal load of 5 N than at a normal load of 2 N. However, the microstructures in Fig. 3g + h and Fig. 6d–i for the SiC/5N/air experiments do not show any evidence of twinning. In contrast, we found DTL formation [4, 5, 13]. The differences between the subsurface microstructures in these two grains are the DTL depths and the grain boundary type of the DTL, which is a SAGB (Fig. 6d) in one grain and a HAGB in the other (Fig. 6g). Additionally, the area between the DTL and the surface is dominated by subgrains in Fig. 6g and does not exhibit a colour-gradient as observed in Fig. 6d. The microstructural features are formed in both grains by dislocation glide and self-organisation. The same was observed and already discussed for the grain in Fig. 3a. Both experiments showed a similar friction coefficient, which also means that the friction force is higher with normal load. This is why the influence of the increased friction force on the DTL depth cannot be separated from the increased normal load. The higher normal load results in a larger misorientation difference at the discontinuities (Figs. 4j, 6j). This can be interpreted as stronger dislocation activity with higher normal forces. Contrary to expectations, an increase in normal load did not increase the twinning probability under tribological load, but rather the amount of dislocation activation and motion.

Dislocation trace line and crystal rotation

Five grains shown in Fig. 3 exhibit a DTL [4, 5, 42] even though their grain orientations and tribological loading differ. Dislocation self-organisation is presumed to be the responsible mechanism for DTL formation [4, 42]. CoCrFeMnNi has a medium SFE [43] resulting in mainly planar slip. It was reported in previous work that these planar slip materials exhibit band-like patterns in the subsurface microstructure after tribological loading [7, 9, 11, 13]. However, exceeding a critical dislocation density might have led here to dislocation self-organisation forming the DTL.

The DTL is only observed in systems with a low friction coefficient and without flake formation in the wear track. The stress state beneath the moving sphere changes with varying friction coefficient [32]. At the same time, the friction force can be interpreted as the sum of forces arising by ploughing and by adhesion [45], with the two being difficult to separate. Therefore, the occurrence of material transfer can further alter the stress state, and to our knowledge, no adequate stress field model exists to cover this behaviour.

The depth of the DTL cannot be correlated with the applied load because the DTL for the experiment SiC/2N/N₂ with the lowest friction coefficient and a normal load of 2N is located at the largest distance to the surface (Fig. 3c). This seems to be contrary to results presented in reference [44], but if the lower and not the upper DTL is considered in [44], the results agree well.

The crystal rotation during tribological loading is an important parameter and can influence the dominant deformation mechanism. The smallest rotation of a crystal direction parallel to a principal sample axis is observed for the crystal direction parallel to TD in Figs. 4 and 6. This means that up to a certain stress level, TD is favoured as rotation axis. The crystal rotation around TD was also observed in other studies [4, 10, 44, 46].

The crystal direction parallel to SD in the SiC/2N/air experiment (Fig. 3g), coloured in dark green, first moves along the [001]–[111] bisector towards the [001] pole with decreasing distance to the surface until [113], where the crystal rotates towards the [001]–[011] bisector. This means that the given rotation changes its direction. This might be explained by a change in glide behaviour as the direction parallel to SD is close to [113] at the turning point. In uniaxial tension or compression experiments, the stacking fault width is independent of the stress state along the line between [012] and [113]. If this line is crossed under uniaxial loading, the stacking fault width either decreases or increases, depending on the applied stress [24]. Further tests are required to identify whether this also holds true for tribological experiments.

Summarising this section, dislocation mediated microstructures of CoCrFeMnNi are caused by low friction coefficients, and they favour the formation of a DTL. The crystal rotation is mainly about TD for low friction coefficients.

Twinning

Besides dislocation activity, also twins were observed. The occurrence of twins can be predicted for uniaxial loading when the crystal orientation is known. This is not the case for a tribological load because of the associated complex stress field.

Three different stages of twinning are observed: The twin in the SiC/2N/air experiment (Fig. 3b) is small, and only one twin system was active. The twin interacts with the surface. The deformation layer in the experiment sapphire/2N/N₂ (Fig. 3d) also shows only one active twin system. However, the twin itself is large and wide, and it does not have any connection to the nanocrystalline layer above. The grain in the Si₃N₄/2N/air experiment (Fig. 3e) exhibits two activated twin systems under similar tribological loading. The twins interact with the SAGB in the near-surface region.

As mentioned in the previous section, the force necessary to activate twinning in the SiC/2N/air experiment (Fig. 3b) is most likely a compression stress parallel to ND. The initial grain direction parallel to ND of the grain featuring twins is not within the [001]–[012]–[113] sector, which precludes twinning under uniaxial compression load. Assuming that the force parallel to ND leads to twinning, the observed crystal rotation towards the [001] pole is necessary for twin formation, as the rotation increases the probability of twinning. Since the twins are small and close to the surface, the twins were most probably formed by slip of Shockley partial dislocations on adjacent {111} planes starting from the surface. This mechanism was observed in MD simulations for nanocrystalline grains [47] and thin films [48]. Further analyses of the MD simulation in [49] given in Figure S1 also show that twins form at the surface under tribological load. The HRTEM image in Fig. 5 suggests the same, as the twin is thicker at the surface. Shockley partial dislocations are nucleated at the surface, and some of them may glide over longer distances than others owing to local differences in the elemental distribution [50]. Steps at the twin boundary are clearly visible and support this hypothesis. In Ref. [16], twinning is observed in Cu under tribological load at high sliding speeds and at cryogenic temperatures, and it is supposed to start at the surface roughness sites as well.

The twins generated in the experiment with sapphire/2N/N₂ and detected using TKD

measurements presented in Fig. 7a–c are of lenticular shape, which is typical of deformation twins in coarse-grained materials. This is an indicator for the Venables mechanism [23] being active.

In the systems discussed so far, only one active twin system was detected, while for $\text{Si}_3\text{N}_4/2\text{N}/\text{air}$ (Fig. 3e), two twin systems are present. In the near-surface region in Fig. 7d–f some SAGBs are visible. The ends of the twins closer to the surface interact with the SAGB. It may be possible that Shockley partial dislocations nucleate at the SAGB and glide on adjacent $\{111\}$ planes, forming the twins. This seems likely as the twins have their largest width at the intersection with the SAGB. Based on MD simulations, easier activation of twinning processes was observed at rough grain boundaries [47], as is the case for the SAGB in Fig. 7d–f. Nevertheless, the Venables twinning mechanism cannot be ruled out completely. It is possible that the twins were nucleated in the bulk region and then interact with the SAGB. Additionally, as mentioned earlier, part of the twin boundary exhibits HAGB characteristics, likely a result from the compounded effect of significant interaction between twin boundary and dislocations. This implies that in the $\text{Si}_3\text{N}_4/2\text{N}/\text{air}$ case not just twin activity, but also twin-boundary–dislocation interaction is high. In addition, the tribological system $\text{Si}_3\text{N}_4/2\text{N}/\text{air}$ with a different initial grain orientation results in the microstructure presented in Fig. 8. Here, neither a DTL nor twins are detected. Instead, a colour-gradient in the TKD measurement is observed and interpreted as crystal rotation [51] caused by dislocation motion. This demonstrates the tremendous influence of the initial grain orientation on the dominant deformation mechanisms.

Based on this discussion, two different types of twins were identified: The first one seems to be caused by compression stresses along ND when Shockley partial dislocations nucleate at the surface and glide on adjacent $\{111\}$ planes. These twins form under lower friction forces and in the absence of material transfer. They are also small in size and width, effectively revealed only via HRTEM and not even by TKD. The second type of twins might arise from the Venables mechanism and be caused by a tensile stress parallel to SD.

Conclusions

We investigated the influence of the friction and the normal force on the dominating deformation mechanisms in CoCrFeMnNi for tribological single-trace experiments. A range of friction forces resulted from selecting varying counter body materials and atmospheres. The use of a polycrystalline material allowed us to give first insights into the role of the initial grain orientation. The ensuing subsurface microstructures were investigated by applying STEM, TKD and HRTEM. The following conclusions can be drawn:

- With the selected tribological systems, dislocation-mediated as well as twinning-induced plasticity microstructures were obtained.
- The dominating deformation mechanism under tribological load is not only dependent on the friction and normal force, but also on the initial grain orientation and the direction of the crystal rotation.
- The responsible force direction and mechanism for deformation twins depends on the tribological loading. With low friction coefficients, the crystal direction parallel to ND seems to be decisive for twin formation. This results in compression twins. These twins are most likely formed by glide of partial dislocations from the surface on adjacent $\{111\}$ planes. With higher friction coefficients, tensile stresses parallel to SD may lead to twinning. These stresses were caused by the adhesive forces and have a tensile character at the trailing edge of the sphere. This means that the crystal orientation has to favour twins under uniaxial tensile load parallel to SD. As these twins are lenticular shaped, they are most likely formed by the Venables mechanism.
- In materials with a medium stacking fault energy such as CoCrFeMnNi, a dislocation trace line (DTL) can be formed, which is unexpected based on the planar slip behaviour. The loading condition most likely influences the degree of the misorientation discontinuity along the DTL.
- Twins are favoured for higher friction forces, and a DTL is preferential at higher normal loads.
- The crystal rotation occurs nearly perfectly around TD at low friction forces.

Acknowledgements

CG acknowledges support by the German Research Foundation (DFG) under Project GR 4174/5-1 as well as by the European Research Council (ERC) under Grant No. 771237, TriboKey. AK thanks financial support by German Research Foundation for grant no. KA 4631/1-1. SJE acknowledges the Austrian COMET-Program (Project K2 InTribology1, no. 872176) and the endowed professorship tribology at the TU Wien (Grant No. WST3-F-5031370/001-2017). LM thanks the Deutscher Akademischer Austauschdienst (DAAD) for a PhD scholarship. The authors acknowledge the chemical analysis by ICP-OES at the Institute for Applied Materials (IAM-AWP), Karlsruhe Institute of Technology (KIT) and the help in sample preparation by Dirk Seifert and Jens Freudenberger, both from IFW Dresden. Computational results were obtained using the Vienna Scientific Cluster (VSC).

Funding

Open Access funding enabled and organized by Projekt DEAL.

Data availability

The data that support the findings in this study are available under the link <https://doi.org/10.5445/IR/100039657> and from the corresponding author upon request.

Declarations

Conflict of interest The authors declare that they have no known competing financial interests or personal relationships that could have appeared to influence the work reported in this paper.

Open Access This article is licensed under a Creative Commons Attribution 4.0 International License, which permits use, sharing, adaptation, distribution and reproduction in any medium or format, as long as you give appropriate credit to the original author(s) and the source, provide a link to the Creative Commons licence, and indicate if changes were made. The images or other third party material in this article are included in the article's Creative Commons

licence, unless indicated otherwise in a credit line to the material. If material is not included in the article's Creative Commons licence and your intended use is not permitted by statutory regulation or exceeds the permitted use, you will need to obtain permission directly from the copyright holder. To view a copy of this licence, visit <http://creativecommons.org/licenses/by/4.0/>.

Supplementary Information: The online version contains supplementary material available at <http://doi.org/10.1007/s10853-022-07661-3>.

References

- [1] Argibay N, Chandross M, Cheng S, Michael JR (2017) Linking microstructural evolution and macro-scale friction behavior in metals. *J Mater Sci* 52:2780–2799. <https://doi.org/10.1007/s10853-016-0569-1>
- [2] Heilmann P, Clark WAT, Rigney DA (1983) Orientation determination of subsurface cells generated by sliding. *Acta Metall* 31:1293–1305. [https://doi.org/10.1016/0001-6160\(83\)90191-8](https://doi.org/10.1016/0001-6160(83)90191-8)
- [3] Rigney DA, Hirth JP (1979) Plastic deformation and sliding friction of metals. *Wear* 53:345–370. [https://doi.org/10.1016/0043-1648\(79\)90087-5](https://doi.org/10.1016/0043-1648(79)90087-5)
- [4] Greiner C, Liu Z, Strassberger L, Gumbsch P (2016) Sequence of stages in the microstructure evolution in copper under mild reciprocating tribological loading. *ACS Appl Mater Interfaces* 8:15809–15819. <https://doi.org/10.1021/acami.6b04035>
- [5] Haug C, Ruebeling F, Kashiwar A, Gumbsch P, Kübel C, Greiner C (2020) Early deformation mechanisms in the shear affected region underneath a copper sliding contact. *Nat Commun* 11:1–8. <https://doi.org/10.1038/s41467-020-14640-2>
- [6] Hughes DA, Hansen N (2001) Graded nanostructures produced by sliding and exhibiting universal behavior. *Phys Rev Lett* 87:135503. <https://doi.org/10.1103/PhysRevLett.87.135503>
- [7] Dollmann A, Kauffmann A, Heilmaier M, Haug C, Greiner C (2020) Microstructural changes in CoCrFeMnNi under mild tribological load. *J Mater Sci* 55:12353. <https://doi.org/10.1007/s10853-020-04806-0>
- [8] Rainforth WM, Stevens R, Nutting J (1992) Deformation structures induced by sliding contact. *Philos Mag A* 66:621–641. <https://doi.org/10.1080/01418619208201580>

- [9] Büscher R, Gleising B, Dudzinski W, Fischer A (2004) The effects of subsurface deformation on the sliding wear behaviour of a microtextured high-nitrogen steel surface. *Wear* 257:284–291. <https://doi.org/10.1016/j.wear.2003.12.013>
- [10] Cai W, Bellon P (2012) Microstructural self-organization triggered by twin boundaries during dry sliding wear. *Acta Mater* 60:6673–6684. <https://doi.org/10.1016/j.actamat.2012.08.037>
- [11] Kim Y-S, Kim S-D, Kim S-J (2007) Effect of phase transformation on wear of high-nitrogen austenitic 18Cr–18Mn–2Mo–0.9N steel. *Mater Sci Eng A* 449–451:1075–1078. <https://doi.org/10.1016/j.msea.2006.02.294>
- [12] Jones MR, Nation BL, Wellington-Johnson JA, Curry JF, Kustas AB, Lu P, Chandross M, Argibay N (2020) Evidence of inverse Hall-Petch behavior and low friction and wear in high entropy alloys. *Sci Rep* 10:10151. <https://doi.org/10.1038/s41598-020-66701-7>
- [13] Liu Z, Messer-Hannemann P, Laube S, Greiner C (2020) Tribological performance and microstructural evolution of α -brass alloys as a function of zinc concentration. *Friction* 8:1117–1136. <https://doi.org/10.1007/s40544-019-0345-8>
- [14] Laube S, Kauffmann A, Ruebeling F, Freudenberger J, Heilmaier M, Greiner C (2020) Solid solution strengthening and deformation behavior of single-phase Cu-base alloys under tribological load. *Acta Mater* 185:300–308. <https://doi.org/10.1016/j.actamat.2019.12.005>
- [15] Emge A, Karthikeyan S, Rigney DA (2009) The effects of sliding velocity and sliding time on nanocrystalline tribolayer development and properties in copper. *Wear* 267:562–567. <https://doi.org/10.1016/j.wear.2008.12.102>
- [16] Chen X, Schneider R, Gumbsch P, Greiner C (2018) Microstructure evolution and deformation mechanisms during high rate and cryogenic sliding of copper. *Acta Mater* 161:138–149. <https://doi.org/10.1016/j.actamat.2018.09.016>
- [17] Rau JS, Balachandran S, Schneider R, Gumbsch P, Gault B, Greiner C (2021) High diffusivity pathways govern massively enhanced oxidation during tribological sliding. *Acta Mater* 221:117353. <https://doi.org/10.1016/j.actamat.2021.117353>
- [18] Cantor B, Chang ITH, Knight P, Vincent AJB (2004) Microstructural development in equiatomic multicomponent alloys. *Mater Sci Eng, A* 375–377:213–218. <https://doi.org/10.1016/j.msea.2003.10.257>
- [19] Otto F, Dlouhý A, Somsen C, Bei H, Eggeler G, George EP (2013) The influences of temperature and microstructure on the tensile properties of a CoCrFeMnNi high-entropy alloy. *Acta Mater* 61:5743–5755. <https://doi.org/10.1016/j.actamat.2013.06.018>
- [20] Laplanche G, Kostka A, Horst OM, Eggeler G, George EP (2016) Microstructure evolution and critical stress for twinning in the CrMnFeCoNi high-entropy alloy. *Acta Mater* 118:152–163. <https://doi.org/10.1016/j.actamat.2016.07.038>
- [21] Ayyagari A, Barthelemy C, Gwalani B, Banerjee R, Scharf TW, Mukherjee S (2017) Reciprocating sliding wear behavior of high entropy alloys in dry and marine environments. *Mater Chem Phys* 210:162–169. <https://doi.org/10.1016/j.matchemphys.2017.07.031>
- [22] Joseph J, Haghdadi N, Shamlaye K, Hodgson P, Barnett M, Fabijanic D (2019) The sliding wear behaviour of CoCrFeMnNi and AlxCoCrFeNi high entropy alloys at elevated temperatures. *Wear* 428–429:32–44. <https://doi.org/10.1016/j.wear.2019.03.002>
- [23] Venables JA (1961) Deformation twinning in face-centred cubic metals. *Phil Mag* 6:379–396. <https://doi.org/10.1080/14786436108235892>
- [24] Karaman I, Sehitoglu H, Gall K, Chumlyakov YI, Maier HJ (2000) Deformation of single crystal Hadfield steel by twinning and slip. *Acta Mater* 48:1345–1359. [https://doi.org/10.1016/S1359-6454\(99\)00383-3](https://doi.org/10.1016/S1359-6454(99)00383-3)
- [25] Tsuya Y (1969) The anisotropy of the coefficient of friction and plastic deformation in copper single crystals. *Wear* 14:309–322. [https://doi.org/10.1016/0043-1648\(69\)90012-X](https://doi.org/10.1016/0043-1648(69)90012-X)
- [26] Prasad SV, Michael JR, Battaile CC, Majumdar BS, Kotula PG (2020) Tribology of single crystal nickel: Interplay of crystallography, microstructural evolution, and friction. *Wear* 458:203320. <https://doi.org/10.1016/j.wear.2020.203320>
- [27] Tarasov SY, Chumaevskii AV, Lychagin DV, Nikonov AY, Dmitriev AI (2018) Subsurface structural evolution and wear lip formation on copper single crystals under unlubricated sliding conditions. *Wear* 410–411:210–221. <https://doi.org/10.1016/j.wear.2018.07.004>
- [28] Xia W, Dehm G, Brinckmann S (2020) Investigation of single asperity wear at the microscale in an austenitic steel. *Wear* 452–453:203289. <https://doi.org/10.1016/j.wear.2020.203289>
- [29] Mayer J, Giannuzzi LA, Kamino T, Michael J (2007) TEM sample preparation and FIB-induced damage. *MRS Bull* 32:400–407. <https://doi.org/10.1557/mrs2007.63>
- [30] Hielscher R, Schaeben H (2008) A novel pole figure inversion method: specification of the MTEX algorithm. *J Appl Cryst, J Appl Crystallogr* 41:1024–1037. <https://doi.org/10.1107/S0021889808030112>
- [31] Kilaas R (1998) Optimal and near-optimal filters in high-resolution electron microscopy. *J Microsc* 190:45–51. <https://doi.org/10.1046/j.1365-2818.1998.3070861.x>
- [32] Hamilton GM, Goodman LE (1966) The stress field created by a circular sliding contact. *J Appl Mech* 33:371–376. <https://doi.org/10.1115/1.3625051>
- [33] ZumGahr K-H (1987) *Microstructure and wear of materials*. Elsevier, Amsterdam

- [34] Kalin M, Polajnar M (2014) The wetting of steel, DLC coatings, ceramics and polymers with oils and water: the importance and correlations of surface energy, surface tension, contact angle and spreading. *Appl Surf Sci* 293:97–108. <https://doi.org/10.1016/j.apsusc.2013.12.109>
- [35] Greenwood JA, Williamson JBP, Bowden FP (1966) Contact of nominally flat surfaces. *Proc R Soc Lond Ser A Math Phys Sci* 295:300–319. <https://doi.org/10.1098/rspa.1966.0242>
- [36] Fuller KNG, Tabor D (1975) The effect of surface roughness on the adhesion of elastic solids. *Proc R Soc Lond A Math Phys Sci* 345:327–342. <https://doi.org/10.1098/rspa.1975.0138>
- [37] Pastewka L, Robbins MO (2016) Contact area of rough spheres: large scale simulations and simple scaling laws. *Appl Phys Lett* 108:221601. <https://doi.org/10.1063/1.4950802>
- [38] Hutchings IM, Shipway P (2017) *Tribology: friction and wear of engineering materials*. Butterworth-Heinemann, Amsterdam
- [39] Bull SJ, Moharrami N, Hainsworth SV, Page TF (2016) The origins of chemomechanical effects in the low-load indentation hardness and tribology of ceramic materials. *J Mater Sci* 51:107–125. <https://doi.org/10.1007/s10853-015-9412-3>
- [40] Buckley DH (1981) *Surface effects in adhesion, friction, wear, and lubrication* -, 1st edn. Elsevier, Amsterdam
- [41] Hansen N, Jensen DJ (1999) Development of microstructure in FCC metals during cold work. *Philos Trans R Soc Lond A Math Phys Eng Sci* 357:1447–1469. <https://doi.org/10.1098/rsta.1999.0384>
- [42] Greiner C, Liu Z, Schneider R, Pastewka L, Gumbsch P (2018) The origin of surface microstructure evolution in sliding friction. *Scr Mater* 153:63–67. <https://doi.org/10.1016/j.scriptamat.2018.04.048>
- [43] Okamoto NL, Fujimoto S, Kambara Y, Kawamura M, Chen ZMT, Matsunoshita H, Tanaka K, Inui H, George EP (2016) Size effect, critical resolved shear stress, stacking fault energy, and solid solution strengthening in the CrMnFeCoNi high-entropy alloy. *Sci Rep* 6:35863. <https://doi.org/10.1038/srep35863>
- [44] Ruebeling F, Xu Y, Richter G, Dini D, Gumbsch P, Greiner C (2021) Normal load and counter body size influence the initiation of microstructural discontinuities in Copper during sliding. *ACS Appl Mater Interfaces*. <https://doi.org/10.1021/acsami.0c19736>
- [45] Bowden FP, Moore AJW, Tabor D (1943) The ploughing and adhesion of sliding metals. *J Appl Phys* 14:80–91. <https://doi.org/10.1063/1.1714954>
- [46] Haug C, Molodov D, Gumbsch P, Greiner C (2022) Tribologically induced crystal rotation kinematics revealed by electron backscatter diffraction. *Acta Mater* 225:117566. <https://doi.org/10.1016/j.actamat.2021.117566>
- [47] Yamakov V, Wolf D, Phillpot SR, Gleiter H (2002) Deformation twinning in nanocrystalline Al by molecular-dynamics simulation. *Acta Mater* 50:5005–5020. [https://doi.org/10.1016/S1359-6454\(02\)00318-X](https://doi.org/10.1016/S1359-6454(02)00318-X)
- [48] Béjaud R, Durinck J, Brochard S (2018) The effect of surface step and twin boundary on deformation twinning in nanoscale metallic systems. *Comput Mater Sci* 145:116–125. <https://doi.org/10.1016/j.commatsci.2017.12.035>
- [49] Eder SJ, RodríguezRipoll M, Cihak-Bayr U, Dini D, Gachot C (2020) Unraveling and mapping the mechanisms for near-surface microstructure evolution in CuNi alloys under sliding. *ACS Appl Mater Interfaces* 12:32197–32208. <https://doi.org/10.1021/acsami.0c09302>
- [50] Smith TM, Hooshmand MS, Esser BD, Otto F, McComb DW, George EP, Ghazisaeidi M, Mills MJ (2016) Atomic-scale characterization and modeling of 60 dislocations in a high-entropy alloy. *Acta Mater* 110:352–363 <https://doi.org/10.1016/j.actamat.2016.03.045>
- [51] Cai W, Bellon P, Beaudoin AJ (2019) Probing the subsurface lattice rotation dynamics in bronze after sliding wear. *Scr Mater* 172:6–11. <https://doi.org/10.1016/j.scriptamat.2019.07.002>
- [52] Stukowski A, Bulatov VV, Arsenlis A (2012) Automated identification and indexing of dislocations in crystal interfaces. *Model Simul Mater Sci Eng* 20:085007. <https://doi.org/10.1088/0965-0393/20/8/085007>

Publisher's Note Springer Nature remains neutral with regard to jurisdictional claims in published maps and institutional affiliations.